Biophysical *Journal*
Article

Biophysical Society

Chloride Anions Regulate Kinetics but Not Voltage-Sensor Q_{max} of the Solute Carrier SLC26a5

Joseph Santos-Sacchi[1,2,3,*] and Lei Song[1]
[1]Department of Surgery (Otolaryngology), [2]Department of Neuroscience, and [3]Department of Cellular and Molecular Physiology, Yale University School of Medicine, New Haven, Connecticut

ABSTRACT In general, SLC26 solute carriers serve to transport a variety of anions across biological membranes. However, prestin (SLC26a5) has evolved, now serving as a motor protein in outer hair cells (OHCs) of the mammalian inner ear and is required for cochlear amplification, a mechanical feedback mechanism to boost auditory performance. The mechanical activity of the OHC imparted by prestin is driven by voltage and controlled by anions, chiefly intracellular chloride. Current opinion is that chloride anions control the Boltzmann characteristics of the voltage sensor responsible for prestin activity, including Q_{max}, the total sensor charge moved within the membrane, and V_h, a measure of prestin's operating voltage range. Here, we show that standard narrow-band, high-frequency admittance measures of nonlinear capacitance (NLC), an alternate representation of the sensor's charge-voltage (Q-V) relationship, is inadequate for assessment of Q_{max}, an estimate of the sum of unitary charges contributed by all voltage sensors within the membrane. Prestin's slow transition rates and chloride-binding kinetics adversely influence these estimates, contributing to the prevalent concept that intracellular chloride level controls the quantity of sensor charge moved. By monitoring charge movement across frequency, using measures of multifrequency admittance, expanded displacement current integration, and OHC electromotility, we find that chloride influences prestin kinetics, thereby controlling charge magnitude at any particular frequency of interrogation. Importantly, however, this chloride dependence vanishes as frequency decreases, with Q_{max} asymptoting at a level irrespective of the chloride level. These data indicate that prestin activity is significantly low-pass in the frequency domain, with important implications for cochlear amplification. We also note that the occurrence of voltage-dependent charge movements in other SLC26 family members may be hidden by inadequate interrogation timescales, and that revelation of such activity could highlight an evolutionary means for kinetic modifications within the family to address hearing requirements in mammals.

INTRODUCTION

Typically, voltage-sensor charge movement in membrane proteins rapidly follows voltage perturbations, producing capacitive-like gating/displacement currents (1,2). However, intrinsic properties of the protein or interactions of the protein with other membrane constituents (protein or lipid) can influence the movement's time course (3). In essence, gating currents may be low-pass filtered relative to the actual driving voltage, often exhibiting multiexponential behavior that depends on the timing of intramolecular and/or intermolecular interactions. Thus, interrogation of charge at other than infinite timescales (or zero frequency) may produce inaccurate quantification of the total charge moved (Q_{max}) across a given cell membrane's electric field where the protein's voltage sensor resides. This issue was recently highlighted by the discovery that previously unidentified slow charge movements, revealed by utilizing longer integration times of 300 ms, account for an apparent charge immobilization in *Shaker* ion channels (4). Importantly, cellular events that result from charge movements may correspondingly be inaccurately assessed.

The family of SLC26 solute carriers functions to maintain gradients of anions across the membranes of a variety of cells (5). However, SLC26a5 (prestin) has been recruited by the outer hair cell (OHC) in Corti's organ to function as a motor protein that underlies cochlear amplification, a mechanical feedback process that boosts auditory sensitivity by 100- to 1000-fold (6,7). OHCs have been shown to produce voltage-dependent length changes (electromotility (eM)) in the audio frequency range (8–10), extending out at least to 80 kHz at room temperature (11). On the other hand, prestin's sensor charge movement, measured as a voltage-dependent or nonlinear capacitance (NLC), displays

Submitted January 26, 2016, and accepted for publication May 4, 2016.

*Correspondence: joseph.santos-sacchi@yale.edu

Lei Song's present address is Department of Otolaryngology Head & Neck Surgery, Shanghai 9th People's Hospital, School of Medicine, Shanghai Jiao Tong University, Shanghai Key Laboratory of Translational Medicine on Ear and Nose Diseases, Shanghai, China.

Editor: Miriam Goodman.

http://dx.doi.org/10.1016/j.bpj.2016.05.002

a limiting frequency, with a cutoff of ~10 kHz at room temperature (12). Thus, the frequency response of the motor protein prestin has differed depending on whether sensor charge or mechanical activity of the protein is evaluated. The expectation that each metric (NLC or eM) should be equivalently fast is based on the assumption that prestin's electromechanical responsiveness to voltage is governed by a direct ultrafast two-state process, switching molecular conformations between compact and expanded states. Thus, technical issues affecting each of these measures could have contributed to the mismatch.

The activity of prestin and its effects on cochlear amplification are strongly dependent on chloride (13–17); it has been shown that alteration of perilymphatic chloride reversibly abolishes cochlear amplification (16). Recently, we observed a dissociation between the eM and NLC magnitude and voltage operating range that we attributed to slow intermediate transitions between prestin's chloride-binding and voltage-enabled states (18). This discrepancy arose because each was evaluated within different frequency regimes (eM at near steady state and NLC at high frequency), under the assumption that the two should have been equivalent. Here, we simultaneously evaluate prestin's charge movement with measures of high-frequency alternating-current (AC) capacitance and step-induced charge integration. We find that quantification of charge is highly dependent on frequency of interrogation, pointing to behavior in prestin that is inconsistent with a simple ultrafast two-state process. Consequently, prestin charge distribution, the rate of which we show to be chloride-dependent, has been wrongly estimated by standard high-frequency AC admittance measures. Voltage-evoked, frequency-dependent eM measurements within the same bandwidth used for NLC measurements confirm these observations. These data reveal that prestin activity is low pass in this frequency domain, and that chloride does not influence Q_{max}, the total prestin charge within the membrane. Our results have significant implications for our current understanding of prestin behavior and cochlear amplification.

MATERIALS AND METHODS

Whole-cell patch-clamp recordings were made from single isolated OHCs from the organs of Corti of Hartley albino guinea pigs. After animals were overdosed with isoflurane, the temporal bones were excised and the top turns of the cochleae dissected free. Enzyme treatment (1 mg/mL Dispase I for 10 min) preceded trituration, and isolated OHCs were placed in a glass-bottom recording chamber. An inverted Nikon (Tokyo, Japan) Eclipse TI-2000 microscope with a 40× lens was used to observe cells during voltage clamping. Experiments were performed at room temperature. Direct-current (DC) voltages were corrected for series-resistance (R_s) effects, and AC currents were corrected for system roll-off, as previously described (19,20). Series and membrane resistance determined from step analysis were similar for the two chloride groups. For the 140 mM Cl group, $R_s = 9.37 \pm 0.31$ MΩ and $R_m = 337 \pm 45.9$ MΩ for $n = 21$ OHCs; for the 1 mM Cl group, $R_s = 8.39 \pm 0.47$ MΩ and $R_m = 365 \pm 40.5$ MΩ for $n = 6$ OHCs. Fig. 5, *G* and *H*, shows that our measurement system, after corrections for R_s effects, is flat out to 5 kHz, within which bandwidth our data arise (see the Appendix in the Supporting Material). All data collection and analysis was done with the software program jClamp (http://www.scisoftco.com).

Solutions

Intracellular chloride levels were set to either 140 or 1 mM, levels that bracket the intracellular concentration found in intact OHCs, namely, ~10 mM (16). An ionic blocking solution was used to remove ionic currents to ensure valid measures of membrane capacitance. The extracellular-base high-Cl solution contained 100 mM NaCl, 20 mM TEA-Cl, 20 mM CsCl, 2 mM $CoCl_2$, 1 mM $MgCl_2$, 1 mM $CaCl_2$, and 10 mM Hepes. In some cases, 1 μM Gd^{3+} was included in the bath solution to block stretch channels and assist in gigohm seal formation. We had previously shown that Gd^{3+} three orders of magnitude greater can block NLC. At the concentration used, no effects on NLC were observed. The intracellular-base solution contained 140 mM CsCl, 2 mM $MgCl_2$, 10 mM Hepes, and 10 mM EGTA. Lower chloride concentrations were set by substituting chloride with gluconate. Intracellular chloride levels in the subplasmalemmal space of the OHC, where prestin's chloride-binding site resides, were guaranteed by setting both intracellular and extracellular chloride concentrations equal. All chemicals used were purchased from Sigma (St. Louis, MO).

Cell capacitance

An Axon Instruments (Foster City, CA) 200B amplifier was used for whole-cell recording. To measure both AC capacitance and integrated charge movement, a simple voltage protocol was designed that included both step stimulation and dual sine stimulation at a range of dual-sine interrogation frequencies (Fig. 1, *A* and *B*). For AC admittance analysis, real and imaginary components of currents were corrected for the recording-system frequency response (19). No averaging was used with this protocol.

Membrane capacitance (C_m) was measured using a continuous dual-frequency (discrete sinusoidal frequencies at f1 and f2, where $f2 = 2 \times f1$) voltage-stimulus protocol (19,21). Simultaneous AC C_m sampling resolutions (5.12, 2.56, 1.28, and 0.064 ms) were achieved by stimulating with a summed multisine voltage (the multi-dual-sine approach) whose phases were the same. Primary frequencies (f1) were 195.3, 390.6, 781.3, and 1562.5 Hz; all frequencies (10 mV peak) were superimposed onto steps from –160 to +100 mV for a duration of 700 ms at a clock sample period of 10 μs. We limited our voltage delivery to −160 to 100 mV because with this protocol, larger voltages caused cell recordings to be lost or unstable. On return from each step to a sinusoidal-free holding potential of 0 mV for at least 40 ms (see Fig. 1, where only a portion of the protocol is plotted), voltage-sensor displacement currents are extractable. Thus, this approach provided both mutlifrequency AC capacitance and step-induced charge movement measures within one protocol, an important approach that ensures that the preparation is quasistationary in time.

After gigohm seal formation, stray capacitance was cancelled with amplifier compensation controls, as is usually done. Since stray capacitance is frequency dependent, it is important to ensure that it is cancelled out at each recording frequency. The existence of stray capacitance causes an apparent frequency dependence of linear capacitance, which should *not* be frequency dependent. Measures of R_s are similarly affected. Consequently, in the whole-cell configuration, residual stray capacitance at each of the recording frequencies was cancelled with further manipulations of amplifier compensation by ensuring that cell linear capacitance (or, equivalently, R_s) was constant across frequency. This was done at very positive voltages, where OHC capacitance is dominated by linear capacitance. Removal of stray capacitance is necessary to meet C_m estimation algorithm requirements (19). We have used this compensation approach to ensure accurate measures of hair cell synaptic vesicle release at high interrogating dual-sine frequencies (20,22). The Supporting Material Appendix expands on our approach.

For each cell, capacitance data were fit to the first derivative of a two-state Boltzmann function with an additional component describing the

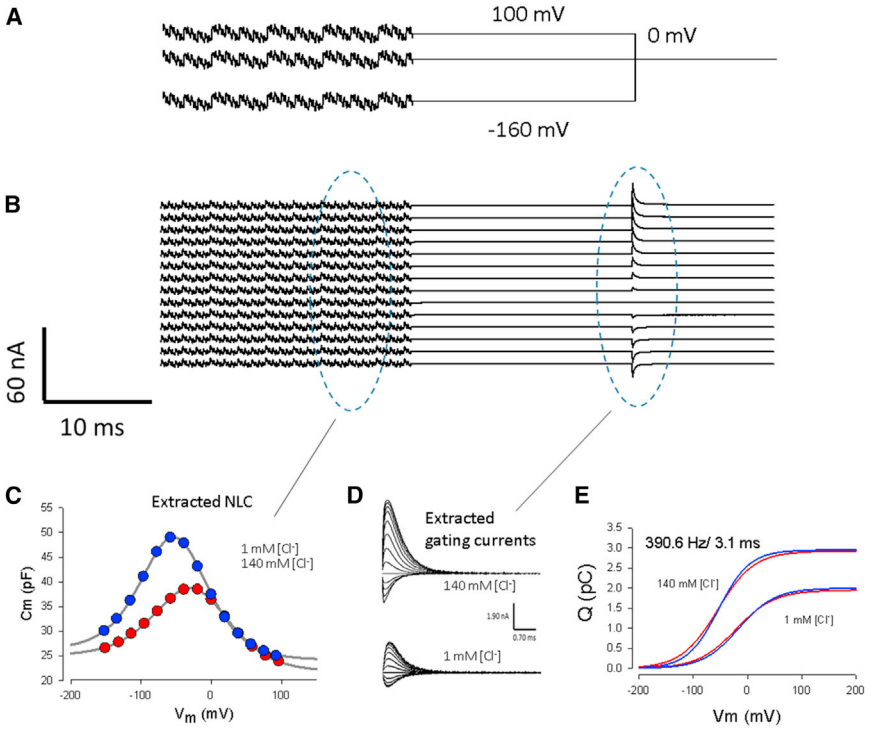

FIGURE 1 Stimulus and analysis paradigms. (*A*) Traces of voltage protocol. Step voltages (−160 mV to +100 mV by 20 mV increments) were delivered for 700 ms followed by a return to a holding potential of 0 mV for 40 ms. Superimposed on the steps were summed discrete dual-sine frequencies 655 ms in duration (see Materials and Methods). (*B*) Elicited currents (offset for easy visualization), AC and step-induced, were used to extract capacitance and integrated charge movements (*dashed ovals*), respectively. (*C*) Averaged NLC traces of OHCs with intracellular chloride clamped to 1 or 140 mM chloride. NLC was estimated from the latter half of the dual-sine stimulation duration. (*D* and *E*) Corresponding displacement currents extracted by linear capacitive current subtraction (*D*) and extracted *Q-V* curves (*E*) at 1 mM and 140 mM chloride conditions for an equivalent interrogation time based on fits of NLC with Eq. 1 (*blue traces*) or on fits of integrated off charge with Eq. 2 (*red traces*) give comparable results, as expected (see Materials and Methods for details). To see this figure in color, go online.

changes in specific membrane capacitance generated by prestin state transitions (23). The occupancy of prestin in the expanded state contributes ~140 zeptofarads/motor (δC_{sa}) to the linear capacitance, producing an apparent voltage-dependent change in linear capacitance at hyperpolarized levels (23,24). This equation is called the two-state-C_{sa} equation.

$$C_m = Q_{max}\frac{ze}{kT}\frac{b}{(1+b)^2} + \frac{\Delta C_{sa}}{(1+b^{-1})} + C_{lin}, \qquad (1)$$

where

$$b = \exp\left(\frac{ze}{kT}U\right) \text{and } U = V_h - V_m.$$

Q_{max} is the maximum nonlinear charge moved, V_h is the voltage at peak capacitance or, equivalently, at half-maximum sensor charge transfer, V_m is the membrane potential, z is valence, e is the electron charge, k is Boltzmann's constant, and T is absolute temperature. C_{lin} is defined as the linear capacitance of the membrane when all prestin motors are in their compact state, the minimum membrane capacitance evident at depolarized voltages; ΔC_{sa} is the maximum increase in capacitance that occurs when all prestin motors change from the compact to the expanded state, each motor contributing a unit response of δC_{sa}. From such fits, voltage-dependent NLC (C_v) is calculated from estimates of Q_{max}, i.e., $C_v = Q_{max}/(4\ kT/ze)$ (25).

To confirm AC admittance estimates of sensor Q_{max}, we integrated capacitive currents evoked at the end of voltage steps (exponentially decaying currents of each trace, with the baseline set to current relaxations at 20 ms). Residual ionic currents that remained after our ionic blocking conditions are time independent and thus were excluded for the most part from integrations of the exponentially decaying currents. The integration time window, starting at voltage offset, was varied from 3 to 20 ms. Previously, we and others used a similar approach that we developed to extract NLC during stair-step protocols by integrating total capacitive current at each step and fitting the resulting C_m-V_m data to a two-state Boltzmann derivative plus a linear capacitance (26,27). Here, *Q-V* curves were fit to the integral of Eq. 1 with respect to V_m, yielding

$$Q_{tot} = \left[\frac{Q_{max} \times b + C_{lin} \times (U + U \times b)}{b+1} + \frac{\Delta C_{sa} \times \log(b+1)}{ze/kT}\right] + \text{off}. \qquad (2)$$

The constant of integration (off) depends on the return holding voltage and accounts for a vertical offset in the Q_{tot}-V_m function. For fitting, we fixed linear capacitance to the average value obtained from AC admittance measures for each chloride group, since these measures provided robust, constant estimates across all frequencies (see Fig. 3). Additionally, we only report measures of integrated charge after 3 ms (10 times our clamp time constant), since earlier charge distribution at the voltage-pulse offset would be influenced by our clamp time constants of <300 μs (~$R_s \times C_m$). With this approach we essentially removed linear capacitive charge contamination from the total integrated charge. Fig. 1 *E* illustrates the equivalence of AC and time-domain estimates of Q_{max}.

Higher resolution of prestin's frequency-dependent behavior was obtained by stimulating OHCs with voltage chirps (linear increasing frequency), with a frequency resolution of 24.41 Hz, and analyzing dual-frequency admittance, obtained by fast Fourier transform, at each component dual frequency (f_1 and $2 \times f_1$). The stimulus consisted of voltage steps (−160 to 160 mV by 40 mV increments) superimposed with voltage chirps of 10 mV peak (4096 points at a 10 μs sampling rate, giving an F_{max} of 50 kHz). One benefit of the chirp signal is that it is a multifrequency stimulus whose individual frequency components are equal in amplitude, this being accomplished by varying the phase of each frequency. Another benefit is that duration of the chirp can be easily changed (although the duration used here was only 40.96 ms). Admittance at one frequency and its harmonic were analyzed in exactly the same way as the dual-sine approach, above (see the Supporting Material Appendix). We do that at all frequencies within the chirp at a primary frequency increment of 24.41 Hz. With this

protocol, filtered responses (10 kHz four-pole Bessel) were averaged three times for each cell to reduce noise. The first chirp response during a step was discarded, since it contains a transient response. We were able to balance out stray capacitance up to a frequency of ~5 kHz. This approach enabled us to construct 3D images of NLC across frequency using averages of all individual cell responses, thereby confirming and expanding on the resolution of the multi-dual-sine approach detailed above.

eM measures

OHC eM data derive from our recent study on the phase relationships of eM and membrane voltage (28). Here, we present the magnitude data transformed into mechanical gain (nm/mV) so that they can be compared to sensor charge movements, i.e., NLC. Briefly, cells were whole-cell voltage clamped and eM was elicited with voltage bursts of frequency ranging from 0.024 to 6 kHz. A photodiode technique was used to measure movements of the apex of the cell, with the cell bound at its basal pole by the patch electrode. Full details can be found in (28).

Kinetic model

A full description of the meno presto model of prestin activity is provided in our recent publications (24,28). Briefly, the model is multistate; after chloride binding, a slow intermediate transition leads to a voltage-enabled state, which generates sensor charge movement. The delays afforded by its multistate nature underlie the model's frequency dependence. The only parameter that was modified to fit (by eye) the data in Fig. 4 was the model's forward transition rate constant, k_1, for Cl^- binding. The kinetic diagram and description are reproduced in Fig. 2 (reproduced from our previous work (24)).

RESULTS

Fig. 1 *C* shows the group-averaged NLC determined from admittance measures (5.12 ms sampling rate) for OHCs recorded under 140 mM and 1 mM intracellular chloride conditions. NLC fits for the 1 mM Cl group yield $V_h = -26.3$ mV, $Q_{max} = 2.2$ pC, $C_{lin} = 21.84$ pF, $z = 0.71$, and $\Delta C_{sa} = 3.2$ pF; those for the 140 mM Cl group yield $V_h = -52.3$ mV, $Q_{max} = 3.1$ pC, $C_{lin} = 24.24$ pF, $z = 0.80$, and $\Delta C_{sa} = 2.1$ pF. Fig. 1 *D* shows voltage-sensor displacement currents after the offset of voltage steps extracted by subtraction of scaled difference currents evoked between the potential of +80 and +100 mV, in an attempt to remove linear capacitive currents, as is required for gating/displacement current extraction (29). Clear chloride differences exist, consistent with expectations. However, because C_m plots show that substantial NLC resides at these subtraction voltages, these displacement currents are inaccurate. We and others have studied OHC/prestin displacement currents for decades (12,30–33); however, because of the shallow voltage dependence of prestin (z ~0.75), extracted waveforms and estimates of Q_{max} using P/N subtraction holding potentials, typically 40–50 mV, were adversely affected in those studies. Extraction of the sensor charge using Eq. 2 (see Materials and Methods) overcomes this problem in determining Q_{max}. Fig. 1 *E* shows that determining Q_{max} with either AC analysis or this time-domain approach produces equivalent results.

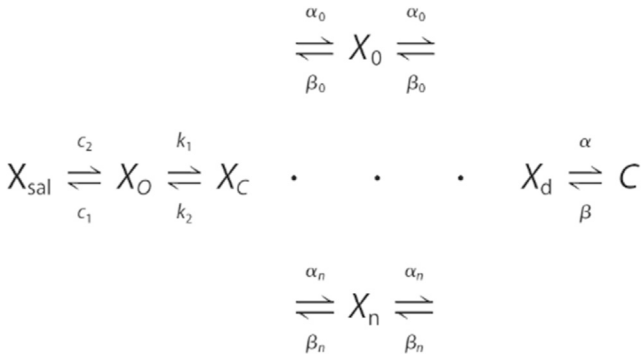

FIGURE 2 Kinetic model of the meno presto model. The X_{sal} state is bound by salicylate, but in this manuscript, salicylate is absent. The X_o state is unbound by an anion. The X_c state is bound by chloride, but the intrinsic voltage-sensor charge is not responsive to the membrane electric field. A slow, multiexponential conformational transition to the X_d state via X_n states enables voltage sensing within the electric field. Depolarization moves the positive sensor charge outward, simultaneously resulting in the compact state, *C*, which corresponds to cell contraction. Parameters and differential equations are provided in (24).

Fig. 3, *A* and *B*, shows group averages of both peak NLC (C_v) and linear capacitance as a function of interrogation frequency. Our success at stray capacitance compensation is borne out by the frequency independence of OHC linear capacitance provided by fits to the C_m data (Fig. 3 *B*). Interestingly, however, NLC shows a marked frequency dependence, with larger magnitudes as interrogating frequency *decreases* (Fig. 3 *A*). In fact, the frequency-dependent trend in C_m data suggests that NLC at frequencies lower than our lowest primary interrogating frequency of 195.3 Hz would be larger. The Boltzmann parameters V_h and z are stable across frequency (Fig. 3, *C* and *D*).

To better compare our measures across cells within the two chloride conditions, we converted our measures to specific nonlinear charge (Q_{sp} in pC/pF), thereby normalizing for surface area and prestin content. In Fig. 4 *A*, we plot AC-derived (Eq. 1) and integration-derived (Eq. 2) sensor charge over a range of interrogation times. Admittance interrogation time refers to the geometric mean of sampling periods of both primary and secondary sinusoids, whereas for integration estimates of sensor displacement charge, interrogation time refers to an integration window increasing up to 20 ms. It can be seen, as predicted from admittance measures alone, that as interrogation time increases, Q_{sp} continuously increases. Integration times >20 ms suffered from excess low-frequency noise, since no averaging could be performed during data collections. Electrode seals were routinely lost after the demanding protocol, since the OHC is quite mechanically active, with responses up to ~30 nm/mV (34) and on average 15 nm/mV (35). To extend our estimates of sensor charge beyond 20 ms, we resorted to measures of averaged electromotility (28), which were analyzed by fast Fourier transform, providing much better signal/noise ratios. Since it is established that eM is voltage-dependent (8,34), sensor charge

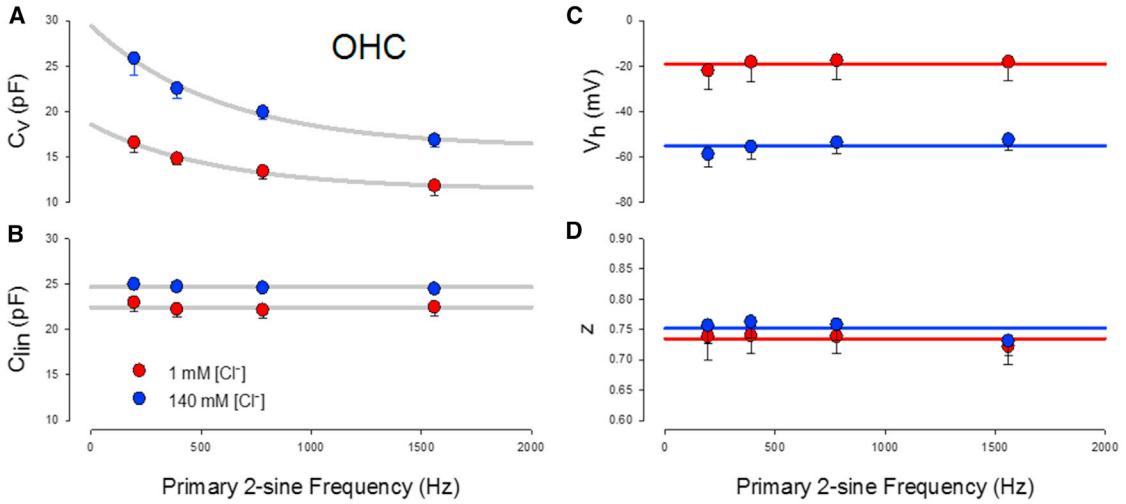

FIGURE 3 Voltage-dependent (C_v) and linear (C_{lin}) components of OHC capacitance simultaneously measured with the multi-dual-sine approach. (*A*) C_v displays a low-pass frequency dependence, which is unexpected for a fast two-state Boltzmann process. Differences between 1 mM (*red circles*, $n = 6$) and 140 mM (*blue circles*, $n = 17$) chloride conditions also show chloride-dependent frequency effects. (*B*) C_{lin} is flat across frequency, as expected. The frequency independence of C_{lin} demonstrates that calibration of system responsiveness was accurately performed. (*C* and *D*) V_h and z are also stable across frequency. Error bars depict the mean ± SE, which in some cases is obscured by symbols. The solid lines in (*A*) are exponential, and those in (*B*)–(*D*) are linear fits for presentation. To see this figure in color, go online.

must correspond to eM magnitude. In Fig. 4 *B*, we plot eM gain as a function of the stimulating-frequency period and show that it corresponds to measures of AC-determined sensor charge. Indeed, eM magnitude continues to grow substantially as interrogation time increases, clearly indicating that sensor charge for both the 140 and 1 mM conditions trends toward equivalence with longer interrogations. These data indicate that total sensor charge movement, Q_{max}, is not directly linked to chloride concentration; rather, only a frequency-dependent, *apparent* Q_{max} is linked, depending on the kinetics of prestin's conformational transitions. It is not necessary to model these data to draw these conclusions.

To understand molecular mechanisms that may underlie this phenomenon, we simulated the meno presto model (initially developed in (18) and expanded with full details in (24)) with the same protocol (Fig. 4 *B*, *gray lines*). As with the biophysical data, charge magnitude is dependent on interrogation time and chloride level. The model fits the data quite well, with increasing integration times (up to 200 ms in the model) incrementally increasing the charge measured. Importantly, for the model, estimated charge at either chloride level asymptotes at the actual set Q_{max}, with the time course depending on prestin's transition rates. Modification of our model parameters (24) was limited to one parameter, namely, a reduction of the model's forward transition rate constant, k_1, for Cl^- binding (from 1e5 to 0.7e4). These results derive from the multiexponential kinetics of sensor charge movement in the meno presto model, some slowly moving charge contributions being missed due to shorter interrogation times, and the fact that only an *apparent* Q_{max} was provided. Such behavior corresponds to our biophysical observations of OHCs and complements the biophysical data, which show that total sensor charge

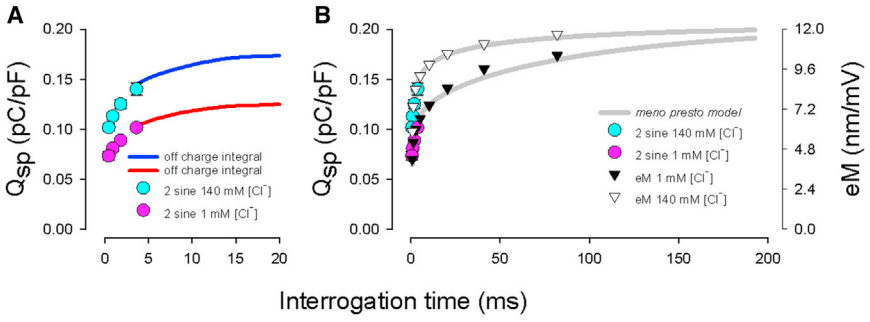

FIGURE 4 Sensor charge movements estimated from two-sine admittance analysis, off-current integration, or eM show low-pass frequency characteristics. (*A*) The AC measured specific sensor charge (Q_{sp}) corresponds to the integrated off-charge and shows that discrete measures of charge movement by AC admittance provide underestimates of the total prestin charge. (*B*) Q_{sp} (*circles*) and eM (*triangles*), which is known to be driven by voltage, display magnitudes that correspond to the predictions of the meno presto model (*gray lines*). Interrogation time is the geometric average of periods of the dual-sine protocol, the integration time of sensor charge, or the eM fundamental frequency period (see Results). The biophysical data and model indicate that regardless of chloride concentration (but at above-zero concentrations), positive voltage will move prestin into the compact state, asymptoting at the maximum sensor charge dictated by prestin membrane content. Data are derived from averages of multi-dual-sine currents (*circles*) and eM (*triangles*) from $n = 5$–8 OHCs. To see this figure in color, go online.

movement is not directly linked to chloride concentration, but rather is misestimated due to prestin kinetics, in contradistinction to long-held concepts.

Finally, to measure prestin's frequency-dependent behavior in finer detail and expand on our data set, we measured NLC using chirp stimuli. Fig. 5 shows averaged results from another group of cells under each of the two chloride conditions (five to six cells per condition). NLC increases with a reduction of interrogating frequency, approaching that expected from zero-frequency or infinite-integration estimates of sensor charge (Fig. 5, *A* and *B*). The meno presto model produces similar results (Fig. 5, *C* and *D*), whereas a fast two-state Boltzmann model and a linear electrical resistor-capacitor (RC) model show no indication of frequency- or voltage/frequency-dependent capacitance, respectively (Fig. 5, *E*, *G*, and *H*). Appropriately setting the rate constants in a two-state model (forward/backward rate constants of 0.5e3 s^{-1}) can produce a frequency-dependent roll-off within the measured bandwidth (Fig. 5 *F*); however, the resulting single-exponential transitions produce a different form of frequency dependence as compared to either the biophysical data or the meno presto model. These data confirm the validity of multi-dual-sine analysis of both linear electrical models and OHC NLC,

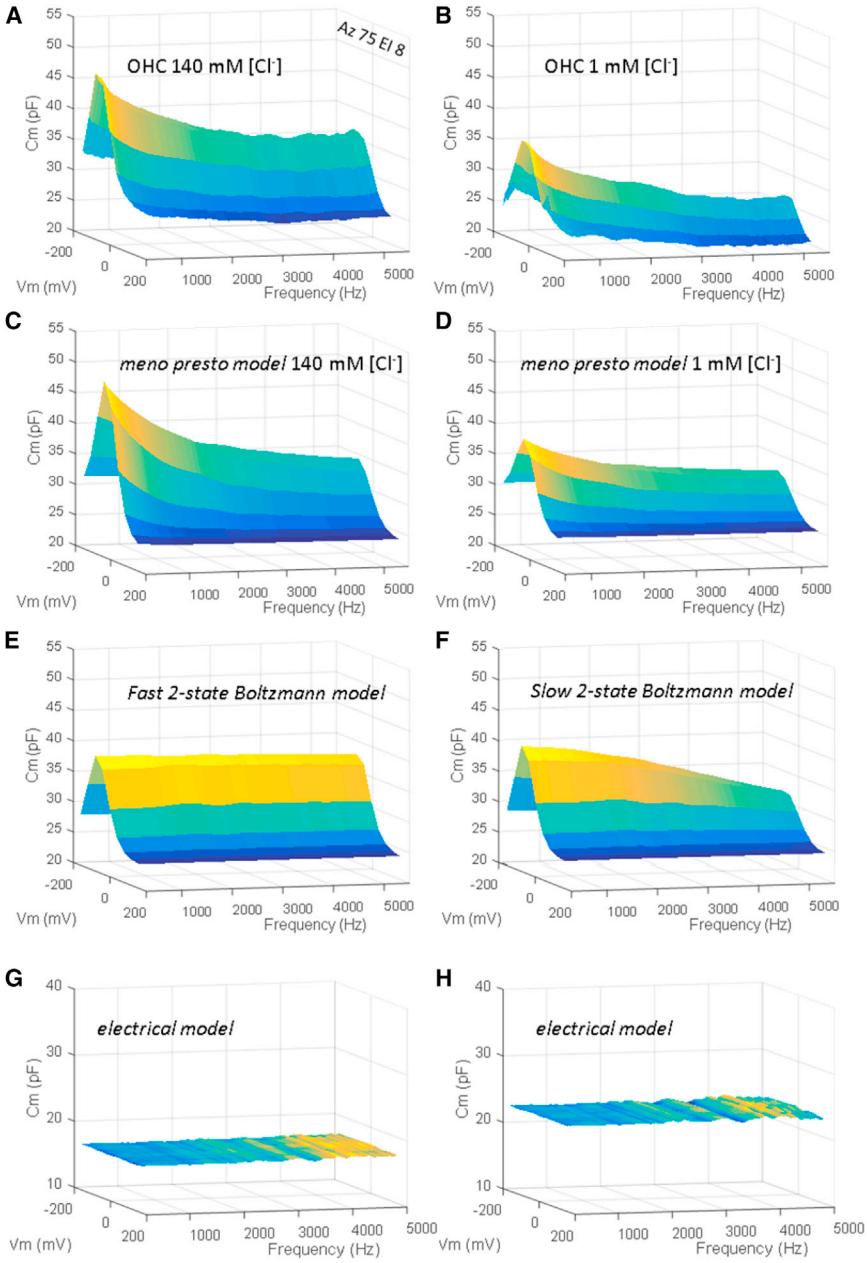

FIGURE 5 Membrane capacitance versus frequency measured by high-resolution frequency-dependent NLC of OHCs, the meno presto model, the fast two-state model, and the electrical model. (*A*) Averaged OHC NLC ($n = 5$) measured using the chirp protocol between 300 and 5000 Hz with 140 mM intracellular chloride. Note the rapid decline of peak capacitance. (*B*) Another group average of OHCs with 1 mM intracellular chloride ($n = 6$). The peak NLC decline is also evident in this condition. (*C* and *D*) C_m versus frequency as measured by the meno presto model at 140 mM and 1 mM chloride, respectively. The stimulus protocol and analysis were the same as the biophysical measures. Note the similarity to the biophysical data. (*E*) C_m versus frequency as measured by the fast two-state Boltzmann model (forward/backward rate constants of 1.5e5 s^{-1}). Note the absence of NLC decline across frequency. (*F*) C_m versus frequency as measured by the slower two-state Boltzmann model (forward/backward rate constants of 0.5e4 s^{-1}). Note the gradual roll-off due to reduced single-exponential transitions. (*G*) C_m versus frequency as measured by the electrical cell model with $R_s = 10$ MΩ, $R_m = 300$ MΩ, $C_m = 17$ pF, all nominal. Note the flat C_m response across frequency and voltage. (*H*) C_m versus frequency as measured by the same electrical model, with an additional 5 pF C_m switched in using a magnetically activated reed relay with minimal additional stray capacitance. To see this figure in color, go online.

highlighting, in the case of the OHC, the need to consider interrogation frequency effects when assessing prestin's voltage-sensor Q_{max}, namely, total sensor charge in a given cell.

DISCUSSION

Characterizing sensor-charge movement in voltage-sensitive proteins provides a host of important information on protein function, including operating voltage range and maximum charge moved (Q_{max}). The latter metric aids in quantifying protein content within the membrane, and our data indicate that prestin may be present at densities higher than the long-held estimates (26,36). For over a decade, chloride has been believed to be a key player in prestin function (13–16), influencing the quantity of measured sensor charge. However, our new data point to a role of chloride in controlling prestin kinetics and not in limiting the quantity of charge movement. Indeed, we previously showed that the maximum OHC eM magnitude, which is expected to correspond to the charge moved, since eM is voltage-driven, is little affected by chloride (18).

Does chloride underlie prestin's voltage-driven charge movement?

Zheng et al. (7) identified the OHC molecular motor as the fifth member of the mammalian SLC26 family of anion exchangers, of which 10 members have been identified (5,37). These anion exchangers facilitate the transmembrane movements of monovalent and divalent anions; however, prestin's transport capabilities are controversial, with some studies showing transport capabilities and others not (38–43). It is interesting to note that the influence of anions on NLC had been observed before the identification of prestin. For example, lipophilic anions, but not cations, were shown to influence OHC eM and NLC (44), and it has been known since the mid 1990s that the anion salicylate blocks NLC and eM, working on the intracellular aspect of the OHC (45,46). Notwithstanding the controversy of anion transport, the existence of voltage-dependent displacement currents, or NLC, has been taken to indicate an evolutionary change that enables eM, since SLC26a5's closest mammalian homolog, SLC26a6, lacks this capability, as assessed by standard high-frequency admittance techniques (13). Whether other SLC26 family members actually possess NLC is a subject for future investigation, since our data indicate that we must now consider the occurrence of charge movements that are slower than typically expected. Should other family members possess slow voltage-sensor charge movements, a scenario wherein kinetic modifications within the family underlie prestin's change to a molecular motor would be compelling. Interestingly, zebra fish prestin shows a lower-pass frequency response than rat prestin (33).

In 2001, Oliver et al. (13) identified the chloride anion as a key element in prestin activation by voltage. They speculated that extrinsic anions serve as prestin's voltage sensor (17), moving only partially through the membrane. Our observations and those of others over the ensuing years have challenged this concept, and we have suggested that chloride works as an allosteric-like modulator of prestin. These observations are as follows. 1) Monovalent, divalent, and trivalent anions, which support NLC, show no expected changes in z or Q_{max} (47). 2) A variety of sulfonic anions shift V_h in widely varying magnitudes and directions along the voltage axis (47). 3) The apparent anion affinity changes depending on the state of prestin, with anions being released from prestin upon hyperpolarization, opposite to the extrinsic sensor hypothesis (48). 4) Mutations of charged residues alter z, our best estimate of unitary sensor charge (41). 5) Prestin shows transport properties ((40,41,43); however, see (39,42)). Despite these challenges, the extrinsic voltage-sensor hypothesis is still entertained. For example, Geertsma et al. (49) used their recently determined crystal structure of SLC26Dg, a prokaryotic fumarate transporter, to speculate on how prestin's extrinsic voltage sensor might work. They reasoned that a switch to an outward-facing state could move a bound anion a small distance within the membrane. Unfortunately, there are no data showing an outward-facing state, only an inward-facing one. Indeed, if prestin did bind chloride but was incapable of reaching the outward-facing state (a defunct transporter), no chloride movements would occur upon voltage perturbation. Furthermore, the fact that the anion-binding pocket is in the center of the protein would mean that if an outward-facing state were achieved with no release of chloride, the monovalent anion would move a very small distance through the electric field of the membrane. However, z, from Boltzmann fits, indicates that the anion moves three-quarters of the distance through the electric field. Unless the electric field is inordinately concentrated only at the binding site, it is difficult to envisage this scenario. The data presented here clearly indicate that no direct relation between chloride level and Q_{max} exists, further suggesting that chloride does not serve as an extrinsic voltage sensor for prestin. Nevertheless, our recent work and meno presto model indicate that chloride binding to prestin is fundamental to the activation of this unusual motor. The model and data indicate that a stretched exponential intermediate transition between the chloride binding and the voltage-enabled state imposes lags that are expressed in whole-cell mechanical responses (28). This intermediate transition also accounts for our frequency- and chloride-dependent effects on measures of total charge movement, Q_{max}. Indeed, based on site-directed mutations of charged residues, we favor intrinsic charges serving as prestin's voltage sensors (41).

Recently, Gorbunov et al. (50), used cysteine accessibility scanning and molecular modeling to suggest structural homology of prestin to UraA. Notably, the crystal structure

of SLC26Dg (49) supports Gorbunov et al.'s structural interpretations of prestin. Given the deduced structure, Gorbunov et al. identified possible chloride-binding residues within prestin's central permeation pathway. When those residues were mutated, the protein became anion-insensitive, yet maintained NLC. For example, in the rPres mutation, R399S, which maintains NLC, salicylate inhibition of NLC was abolished. These data are in line with our observations that truncated Cl^- movements are not responsible for voltage sensing, namely, the generation of NLC.

We suggest, instead, that various anions differentially modulate the transition rates of prestin, likely as a consequence of their different binding affinities, thereby influencing V_h (i.e., the distribution of compact and expanded states of prestin) and the *apparent* Q_{max} obtained via discrete frequency admittance measures. This concept may explain the wide variability in prestin's Boltzmann parameters that we and others have found with various anions (13,47).

Some of prestin's voltage-dependent characteristics are inadequately assessed using admittance analysis

The prevailing concept of prestin activity has been that of an ultrafast two-state Boltzmann process. This is not surprising, since the OHC can change its length at acoustic rates up to 80 kHz (8–11). Consequently, this reasoning has guided our assessment method of prestin activity, where AC NLC measures have usurped the more tedious gating-current methods that were utilized early on (32,35,51). Nevertheless, even gating-charge evaluations have suffered from problems associated with inadequate integration times and the shallow voltage dependence of prestin, which makes adequate linear leakage subtraction nearly impossible. Our data now show that AC capacitance measures do not correspond to full motor capability (18). The inaccuracies that fast single or dual AC measurements provide needn't preclude their use, however, now that we have uncovered their limitations. Thus, by measuring C_m with a range of frequencies, with proper calibration for stray capacitance effects and including long interrogation times, valid measures of Q_{max} can be obtained.

We previously noted that Boltzmann fits to the *Q-V* function of prestin cannot reliably predict unitary motor charge, Q_m, since even Langevin fits are reasonable, which would place Q_m values 3 times higher relative to two-state fits (26). This has been clearly emphasized by the Gummer group (52). One outcome of our study indicates that regardless of unitary charge magnitude (which remains stable across frequency, as indicated by invariant z values), the larger Q_{max} estimates from long interrogation times point to a higher density of prestin within the OHC lateral membrane. Consequently, the changes in prestin charge density observed in previous studies by narrow-band admittance techniques may have been due to the effects of altered kinetics rather than prestin membrane content.

Frequency dependence of OHC charge movement

The frequency dependence of OHC charge movement has been investigated previously (12,31). Using the methodology of Fernandez et al. (53), we showed that capacitive reactance of the OHC with 140 mM intracellular solution in the whole-cell voltage-clamp configuration was voltage- and frequency-dependent, rising as zero frequency was approached (31). Subsequently, Gale and Ashmore (12) measured NLC in OHC membrane patches, where clamp time constants were better suited to high-frequency assessment. They found flat responses out to ~10 kHz at room temperature. Importantly, the direct effects of temperature on OHC displacement currents and NLC have been evaluated and shown to substantially affect NLC V_h (indicative of transition-rate effects) of both OHC and prestin-transfected cells when the bath temperature is altered (30,54,55). Shifts of ~20 mV/°C were found. Additionally, temperature jumps using an infrared laser on prestin-transfected cells (56) induced C_m changes attributable to NLC as well as linear C_m, as originally described by Shapiro et al. (57). NLC V_h shifted with rates up to 14 V/s over the course of a 5 ms infrared pulse. Thus, it is clear that temperature will influence the frequency dependence of OHC NLC. Consequently, after correcting for temperature, Gale and Ashmore (12) arrived at a 25 kHz cutoff for NLC, still far below the eM cutoff observed at room temperature (11). We suggest that these incompatible measures arise from technical issues. Considering the characteristics of our recently espoused meno presto model (24,28), we further suggest that sufficiently long stimulations of the OHC will drive substantial numbers of prestins into the chloride-bound, voltage-enabled state where they may rapidly respond to voltage perturbations with cutoff frequencies possibly unencumbered by the chloride-binding step. Thus, the performance of the OHC may modulate between two frequency regimes, high and low; the latter likely related to a slow transport function of the protein (40,41,43).

Recently, Homma et al. (58) have measured the frequency dependence of OHC NLC using our dual-sine approach, but only with discrete dual-sine frequencies and without presentation of linear capacitance data. Interestingly, they found that NLC in control mouse OHCs was frequency *independent* with high intracellular iodide solutions, but frequency *dependent* with high intracellular chloride conditions. The latter results are similar to our results under high-chloride conditions. Thus, we concur that anions are influential in controlling prestin kinetics, and we now must consider the effects of chloride substitutes on prestin kinetics. Here, we used gluconate—previously confirmed to be similar to aspartate substitution (18)—to lower chloride to near

physiological levels (16). Whether any of the effects of iodide were due to chloride reductions remains to be investigated.

Interestingly, Albert et al. (33) also presented data showing low-pass NLC activity in rat prestin using single-sine measurements (see their Fig. 3 *E*), which they attributed to their recording equipment. Yet they note very fast clamp speeds, and furthermore, they do not claim any untoward influences on the low-pass nature of zebra fish prestin in that same study.

How can low-pass prestin sensor charge movement that directly drives eM underlie cochlear amplification?

Cochlear amplification provides a boost to auditory sensitivity ranging from 100- to 1000-fold. It is thought to be maximal at high acoustic frequencies, in the tens of kilohertz range. There is ample evidence that prestin-driven OHC electromechanical activity underlies cochlear amplification, yet how can a voltage-dependent process that relies on a low-pass voltage sensor to drive mechanical activity work? We have previously estimated that mechanical responses at high acoustic frequencies would be markedly smaller than basilar motion, based on the cell's RC time constant. This problem has been addressed by many investigators, and many ostensible resolutions to the RC time-constant problem have been proposed (15,25,59–62). However, we must now consider the slow kinetics of prestin at physiological chloride levels that we have uncovered. This can only make matters worse. To be sure, we have recently found that eM magnitude rolls off faster than membrane voltage (28), and now we show that this roll-off corresponds to sensor charge activity (Fig. 4 *B*). It is possible that eM is not the main player and that OHC voltage-dependent stiffness, for which there is a wealth of evidence (63–65), is important.

On the other hand, we have found that the low-pass kinetic features of prestin can have high-frequency effects that could influence its ability to interact with basilar membrane/cochlear partition mechanics. Notably, we recently found a frequency-dependent phase lag in eM (re voltage) that is chloride dependent and is attributable to prestin's multistate kinetic features (28). Interestingly, phase lags are also predicted based on an electrodiffusion model of prestin (66), although the group that made that prediction suggested through additional modeling that power-law viscoelastic properties of the membrane could counter the effects of such lags (67). Whether such unusual viscoelastic properties characterize prestin's membrane environment is not known; however, our measured eM phase behavior in OHCs suggests no countering effects of viscoelasticity in the frequency range we studied. We propose that an accumulating phase lag at the molecular level could have a significant influence on the OHC's ability to inject power into the cochlear partition, despite an associated magnitude roll-off dictated by low-pass sensor charge movement.

SUPPORTING MATERIAL

Supporting Materials and Methods and three figures are available at http://www.biophysj.org/biophysj/supplemental/S0006-3495(16)30278-8.

AUTHOR CONTRIBUTIONS

J.S.S. designed and performed experiments, analyzed data, and wrote the article. LS performed experiments.

ACKNOWLEDGMENTS

This research was supported by National Institutes of Health National Institute on Deafness and Other Communication Disorders grants DC00273 and DC008130 to J.S.S.

REFERENCES

1. Armstrong, C. M., and F. Bezanilla. 1973. Currents related to movement of the gating particles of the sodium channels. *Nature.* 242:459–461.
2. Schneider, M. F., and W. K. Chandler. 1973. Voltage dependent charge movement of skeletal muscle: a possible step in excitation-contraction coupling. *Nature.* 242:244–246.
3. Bezanilla, F. 2008. How membrane proteins sense voltage. *Nat. Rev. Mol. Cell Biol.* 9:323–332.
4. Lacroix, J. J., A. J. Labro, and F. Bezanilla. 2011. Properties of deactivation gating currents in *Shaker* channels. *Biophys. J.* 100:L28–L30.
5. Alper, S. L., and A. K. Sharma. 2013. The SLC26 gene family of anion transporters and channels. *Mol. Aspects Med.* 34:494–515.
6. Ruggero, M. A., and N. C. Rich. 1991. Furosemide alters organ of Corti mechanics: evidence for feedback of outer hair cells upon the basilar membrane. *J. Neurosci.* 11:1057–1067.
7. Zheng, J., W. Shen, …, P. Dallos. 2000. Prestin is the motor protein of cochlear outer hair cells. *Nature.* 405:149–155.
8. Ashmore, J. F. 1987. A fast motile response in guinea-pig outer hair cells: the cellular basis of the cochlear amplifier. *J. Physiol.* 388:323–347.
9. Santos-Sacchi, J. 1992. On the frequency limit and phase of outer hair cell motility: effects of the membrane filter. *J. Neurosci.* 12:1906–1916.
10. Dallos, P., and B. N. Evans. 1995. High-frequency motility of outer hair cells and the cochlear amplifier. *Science.* 267:2006–2009.
11. Frank, G., W. Hemmert, and A. W. Gummer. 1999. Limiting dynamics of high-frequency electromechanical transduction of outer hair cells. *Proc. Natl. Acad. Sci. USA.* 96:4420–4425.
12. Gale, J. E., and J. F. Ashmore. 1997. An intrinsic frequency limit to the cochlear amplifier. *Nature.* 389:63–66.
13. Oliver, D., D. Z. He, …, B. Fakler. 2001. Intracellular anions as the voltage sensor of prestin, the outer hair cell motor protein. *Science.* 292:2340–2343.
14. Song, L., A. Seeger, and J. Santos-Sacchi. 2005. On membrane motor activity and chloride flux in the outer hair cell: lessons learned from the environmental toxin tributyltin. *Biophys. J.* 88:2350–2362.
15. Rybalchenko, V., and J. Santos-Sacchi. 2003. Cl^- flux through a non-selective, stretch-sensitive conductance influences the outer hair cell motor of the guinea-pig. *J. Physiol.* 547:873–891.

16. Santos-Sacchi, J., L. Song, …, A. L. Nuttall. 2006. Control of mammalian cochlear amplification by chloride anions. *J. Neurosci.* 26:3992–3998.

17. Oliver, D., T. Schächinger, and B. Fakler. 2006. Interaction of prestin (SLC26A5) with monovalent intracellular anions. *Novartis Found. Symp.* 273:244–253, discussion 253–260, 261–264.

18. Song, L., and J. Santos-Sacchi. 2013. Disparities in voltage-sensor charge and electromotility imply slow chloride-driven state transitions in the solute carrier SLC26a5. *Proc. Natl. Acad. Sci. USA.* 110:3883–3888.

19. Santos-Sacchi, J. 2004. Determination of cell capacitance using the exact empirical solution of ∂Y/∂Cm and its phase angle. *Biophys. J.* 87:714–727.

20. Schnee, M. E., J. Santos-Sacchi, …, A. J. Ricci. 2011. Calcium-dependent synaptic vesicle trafficking underlies indefatigable release at the hair cell afferent fiber synapse. *Neuron.* 70:326–338.

21. Santos-Sacchi, J., S. Kakehata, and S. Takahashi. 1998. Effects of membrane potential on the voltage dependence of motility-related charge in outer hair cells of the guinea-pig. *J. Physiol.* 510:225–235.

22. Schnee, M. E., M. Castellano-Muñoz, …, A. J. Ricci. 2011. Tracking vesicle fusion from hair cell ribbon synapses using a high frequency, dual sine wave stimulus paradigm. *Commun. Integr. Biol.* 4:785–787.

23. Santos-Sacchi, J., and E. Navarrete. 2002. Voltage-dependent changes in specific membrane capacitance caused by prestin, the outer hair cell lateral membrane motor. *Pflugers Arch.* 444:99–106.

24. Santos-Sacchi, J., and L. Song. 2014. Chloride and salicylate influence prestin-dependent specific membrane capacitance: support for the area motor model. *J. Biol. Chem.* 289:10823–10830.

25. Santos-Sacchi, J., S. Kakehata, …, T. Takasaka. 1998. Density of motility-related charge in the outer hair cell of the guinea pig is inversely related to best frequency. *Neurosci. Lett.* 256:155–158.

26. Huang, G., and J. Santos-Sacchi. 1993. Mapping the distribution of the outer hair cell motility voltage sensor by electrical amputation. *Biophys. J.* 65:2228–2236.

27. Oliver, D., and B. Fakler. 1999. Expression density and functional characteristics of the outer hair cell motor protein are regulated during postnatal development in rat. *J. Physiol.* 519:791–800, (In Process Citation).

28. Santos-Sacchi, J., and L. Song. 2014. Chloride-driven electromechanical phase lags at acoustic frequencies are generated by SLC26a5, the outer hair cell motor protein. *Biophys. J.* 107:126–133.

29. Bezanilla, F., and C. M. Armstrong. 1977. Inactivation of the sodium channel. I. Sodium current experiments. *J. Gen. Physiol.* 70:549–566.

30. Santos-Sacchi, J., and G. Huang. 1998. Temperature dependence of outer hair cell nonlinear capacitance. *Hear. Res.* 116:99–106.

31. Santos-Sacchi, J. 1991. Reversible inhibition of voltage-dependent outer hair cell motility and capacitance. *J. Neurosci.* 11:3096–3110.

32. Ashmore, J. F. 1989. Transducer motor coupling in cochlear outer hair cells. *In* Mechanics of Hearing. D. Kemp and J. P. Wilson, editors. Plenum Press, New York, pp. 107–113.

33. Albert, J. T., H. Winter, …, D. Oliver. 2007. Voltage-sensitive prestin orthologue expressed in zebrafish hair cells. *J. Physiol.* 580:451–461.

34. Santos-Sacchi, J., and J. P. Dilger. 1988. Whole cell currents and mechanical responses of isolated outer hair cells. *Hear. Res.* 35:143–150.

35. Santos-Sacchi, J. 1989. Asymmetry in voltage-dependent movements of isolated outer hair cells from the organ of Corti. *J. Neurosci.* 9:2954–2962.

36. Gale, J. E., and J. F. Ashmore. 1997. The outer hair cell motor in membrane patches. *Pflugers Arch.* 434:267–271.

37. Mount, D. B., and M. F. Romero. 2004. The SLC26 gene family of multifunctional anion exchangers. *Pflugers Arch.* 447:710–721.

38. Schaechinger, T. J., D. Gorbunov, …, D. Oliver. 2011. A synthetic prestin reveals protein domains and molecular operation of outer hair cell piezoelectricity. *EMBO J.* 30:2793–2804.

39. Schaechinger, T. J., and D. Oliver. 2007. Nonmammalian orthologs of prestin (SLC26A5) are electrogenic divalent/chloride anion exchangers. *Proc. Natl. Acad. Sci. USA.* 104:7693–7698.

40. Mistrík, P., N. Daudet, …, J. F. Ashmore. 2012. Mammalian prestin is a weak Cl^-/HCO_3^- electrogenic antiporter. *J. Physiol.* 590:5597–5610.

41. Bai, J. P., A. Surguchev, …, D. Navaratnam. 2009. Prestin's anion transport and voltage-sensing capabilities are independent. *Biophys. J.* 96:3179–3186.

42. Tan, X., J. L. Pecka, …, D. Z. He. 2011. From zebrafish to mammal: functional evolution of prestin, the motor protein of cochlear outer hair cells. *J. Neurophysiol.* 105:36–44.

43. Schänzler, M., and C. Fahlke. 2012. Anion transport by the cochlear motor protein prestin. *J. Physiol.* 590:259–272.

44. Wu, M., and J. Santos-Sacchi. 1998. Effects of lipophilic ions on outer hair cell membrane capacitance and motility. *J. Membr. Biol.* 166:111–118.

45. Kakehata, S., and J. Santos-Sacchi. 1996. Effects of salicylate and lanthanides on outer hair cell motility and associated gating charge. *J. Neurosci.* 16:4881–4889.

46. Tunstall, M. J., J. E. Gale, and J. F. Ashmore. 1995. Action of salicylate on membrane capacitance of outer hair cells from the guinea-pig cochlea. *J. Physiol.* 485:739–752.

47. Rybalchenko, V., and J. Santos-Sacchi. 2008. Anion control of voltage sensing by the motor protein prestin in outer hair cells. *Biophys. J.* 95:4439–4447.

48. Song, L., and J. Santos-Sacchi. 2010. Conformational state-dependent anion binding in prestin: evidence for allosteric modulation. *Biophys. J.* 98:371–376.

49. Geertsma, E. R., Y. N. Chang, …, R. Dutzler. 2015. Structure of a prokaryotic fumarate transporter reveals the architecture of the SLC26 family. *Nat. Struct. Mol. Biol.* 22:803–808.

50. Gorbunov, D., M. Sturlese, …, D. Oliver. 2014. Molecular architecture and the structural basis for anion interaction in prestin and SLC26 transporters. *Nat. Commun.* 5:3622.

51. Santos-Sacchi, J. 1990. Fast outer hair cell motility: how fast is fast? *In* The Mechanics and Biophysics of Hearing. P. Dallos, C. D. Geisler, J. W. Matthews, M. A. Ruggero, and C. R. Steele, editors. Springer-Verlag, Berlin, pp. 69–75.

52. Scherer, M. P., and A. W. Gummer. 2005. How many states can the motor molecule, prestin, assume in an electric field? *Biophys. J.* 88:L27–L29.

53. Fernández, J. M., F. Bezanilla, and R. E. Taylor. 1982. Distribution and kinetics of membrane dielectric polarization. II. Frequency domain studies of gating currents. *J. Gen. Physiol.* 79:41–67.

54. Santos-Sacchi, J., L. Song, and X. T. Li. 2009. Firing up the amplifier: temperature, pressure and voltage jump studies on ohc motor capacitance. *In* Proceedings of the International Workshop on the Mechanics of Hearing (Keele University): 363–370.

55. Meltzer, J., and J. Santos-Sacchi. 2001. Temperature dependence of non-linear capacitance in human embryonic kidney cells transfected with prestin, the outer hair cell motor protein. *Neurosci. Lett.* 313:141–144.

56. Okunade, O., and J. Santos-Sacchi. 2013. IR laser-induced perturbations of the voltage-dependent solute carrier protein SLC26a5. *Biophys. J.* 105:1822–1828.

57. Shapiro, M. G., M. F. Priest, …, F. Bezanilla. 2013. Thermal mechanisms of millimeter wave stimulation of excitable cells. *Biophys. J.* 104:2622–2628.

58. Homma, K., C. Duan, …, P. Dallos. 2013. The V499G/Y501H mutation impairs fast motor kinetics of prestin and has significance for defining functional independence of individual prestin subunits. *J. Biol. Chem.* 288:2452–2463.

59. Ospeck, M., X. X. Dong, …, K. H. Iwasa. 2006. Electromotility in outer hair cells: a supporting role for fast potassium conductance. *ORL J. Otorhinolaryngol. Relat. Spec.* 68:373–377.

60. Spector, A. A., W. E. Brownell, and A. S. Popel. 2003. Effect of outer hair cell piezoelectricity on high-frequency receptor potentials. *J. Acoust. Soc. Am.* 113:453–461.

61. Johnson, S. L., M. Beurg, …, R. Fettiplace. 2011. Prestin-driven cochlear amplification is not limited by the outer hair cell membrane time constant. *Neuron.* 70:1143–1154.

62. Corbitt, C., F. Farinelli, …, B. Farrell. 2012. Tonotopic relationships reveal the charge density varies along the lateral wall of outer hair cells. *Biophys. J.* 102:2715–2724.

63. He, D. Z., S. Jia, and P. Dallos. 2003. Prestin and the dynamic stiffness of cochlear outer hair cells. *J. Neurosci.* 23:9089–9096.

64. He, D. Z., and P. Dallos. 2000. Properties of voltage-dependent somatic stiffness of cochlear outer hair cells. *J. Assoc. Res. Otolaryngol.* 1:64–81.

65. He, D. Z., and P. Dallos. 1999. Somatic stiffness of cochlear outer hair cells is voltage-dependent. *Proc. Natl. Acad. Sci. USA.* 96:8223–8228.

66. Sun, S. X., B. Farrell, …, A. A. Spector. 2009. Voltage and frequency dependence of prestin-associated charge transfer. *J. Theor. Biol.* 260:137–144.

67. Roy, S., W. E. Brownell, and A. A. Spector. 2012. Modeling electrically active viscoelastic membranes. *PLoS One.* 7:e37667.

Biophysical Journal, Volume *110*

Supplemental Information

Chloride Anions Regulate Kinetics but Not Voltage-Sensor Q_{max} of the Solute Carrier SLC26a5

Joseph Santos-Sacchi and Lei Song

Supporting material

Removal of stray capacitance at C_m measuring frequencies

We use an Axon 200B patch clamp amplifier to measure OHC capacitance. Methodology was coded in jClamp and utilizes admittance measures at 2 frequencies to measure capacitance (1, 2). A linear cell model is depicted below, where Rs, Rm and Cm at each frequency (ω0, ω1) are derived from the following equations.

a0=real(Y) @ w0
a1=real(Y) @ w1
b0=imag(Y) @ w0
b1=imag(Y) @ w1

c0=a0^2 + b0^2;
c1=a1^2 + b1^2;

*b=(-0.5) * (-c1+c0 + sqrt(c1^2 - 2*c1*c0 + c0^2 - 4*a1*a0*c1 + 4*a1^2*c0 + 4*a0^2*c1 - 4*a0*a1*c0)) / (a1-a0);*

*Rs0=(a0-b) ./ (a0.^2 + b0.^2 - a0*b);*
*Rm0=1/b * ((a0-b).^2 + b0.^2) ./ (a0.^2 + b0.^2 - a0*b);*
Cm0=((1 ./ (w0. b0)) .* ((a0.^2 + b0.^2 - a0*b).^2) ./ ((a0-b).^2 + b0.^2));*

*Rs1=(a1-b) ./ (a1.^2 + b1.^2 - a1*b);*
*Rm1=1/b * ((a1-b).^2 + b1.^2) ./ (a1.^2 + b1.^2 - a1*b);*
Cm1=(1 ./ (w1. b1)) .* ((a1.^2 + b1.^2 - a1*b).^2 ./ ((a1-b).^2 + b1.^2));*

An example of our approach to remove stray capacitance is shown below using jClamp interfaced to a MatLab Simulink model. First, the model is evaluated without stray capacitance, where Rs= 10 Mohm, Rm=200 Mohm, Cm= 15 pF.

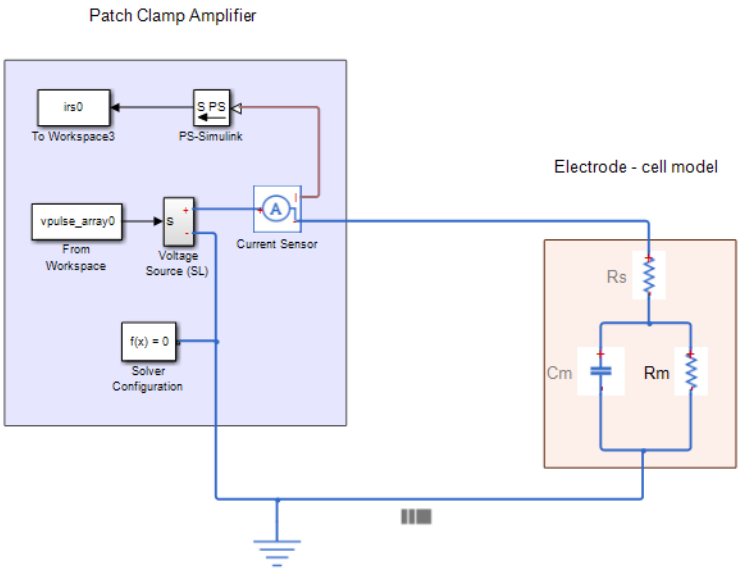

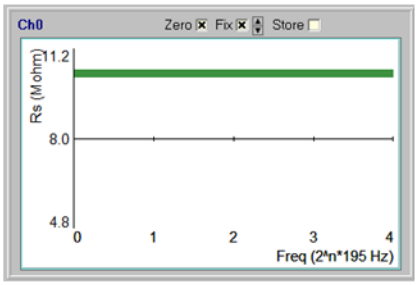

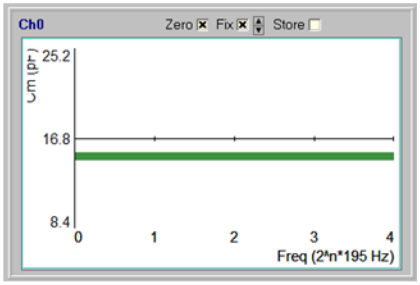

Note that the solutions (Rs and Cm plotted) provide exact parameter estimates regardless of frequency of stimulation (or, in fact, regardless of component values). However, real world recording includes parasitic capacitances, termed stray capacitance, the inclusion of which is modeled below.

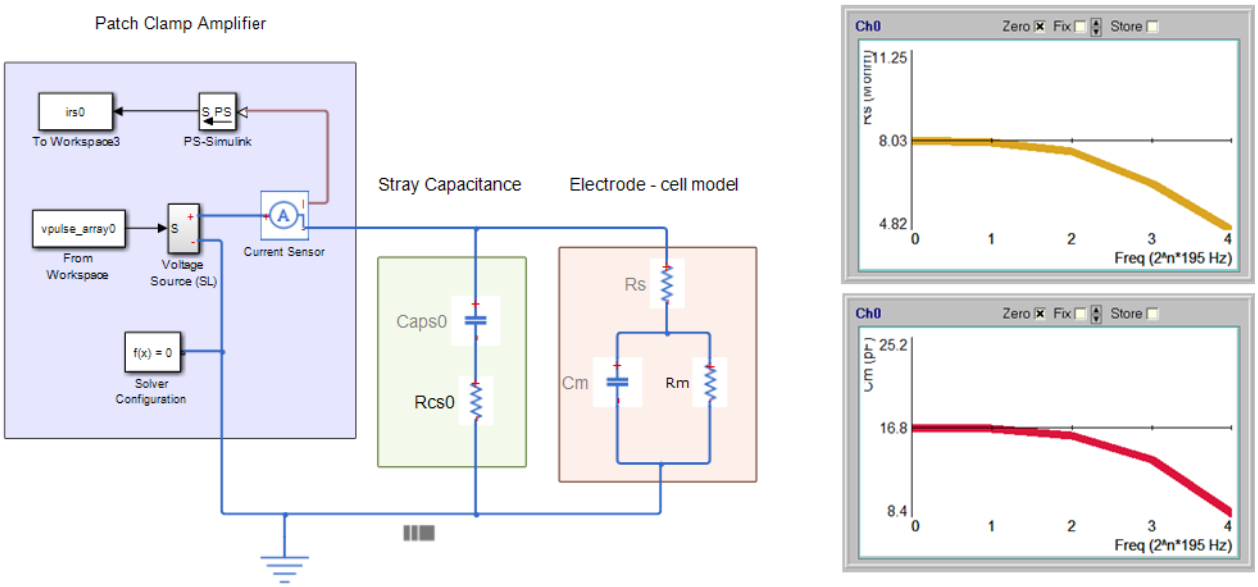

Here, utilization of the exact solutions above provides inaccurate measures, showing both Rs and Cm decreasing with increasing frequency. Both Rs and Cm are linear, and as defined are neither frequency nor voltage dependent. It behooves us then to remove stray capacitance effects during our recordings, since only without stray capacitance are our equations valid. Typically, stray capacitance effects (e.g., due to pipette holder and pipette – we use thick wall borosilicate glass pipettes coated with M-coat to reduce stray capacitance) are cancelled following gigohm seal formation during patch clamp recording by utilizing Axon 200B amplifier capacitance compensation controls. Unfortunately, this balancing procedure (using voltage steps in the time domain to cancel capacitive spikes) often is imperfect and stray capacitance effects can remain at our measurement frequencies. We attempt to overcome this problem after establishing whole cell configuration by stimulating in the frequency domain with a multi-frequency protocol that defines our interrogating frequencies. We then further fine balance with amplifier controls until calculated linear Cm and Rs are flat across frequency, as they should be. Any change in stray capacitance during the course of a recording session can be cancelled in this manner, e.g., if bath fluid levels changes. For our studies on synaptic activity (3-5), we can remove stray capacitance at any holding potential since the membranes of cells we study have no large intrinsic voltage dependent capacitance. However, in order to balance out stray capacitance for OHCs we hold the cell at positive potentials where linear capacitance dominates. Having succeeded in minimizing confounding effects of stray capacitance on linear membrane capacitance measurements across frequency, we then can investigate the frequency dependence of **NLC**. As detailed in the *Methods* section of our manuscript, Cm is measured at a range of holding potentials to generate a Cm-Vm plot that is fit with *eq. 1*, enabling extraction of Boltzmann characteristics, Qmax, Vh, and z. When sensor charge (Qmax) is plotted versus frequency of interrogation, we find that **NLC** is frequency dependent but linear capacitance is frequency independent (Fig. 2), confirming stray capacitance cancellation at our measuring frequencies. Our modelling indicates that the frequency dependence of **NLC** relates to the transition rates between conformational states of prestin.

Rs effects on membrane voltage drop and clamp time constant are removed with our methodology

Equipment frequency response (magnitude and phase of amplifier and associated equipment in the recording path) is corrected for by generating a calibration table across measurement frequencies, which is applied post-hoc to correct data for system response characteristics. This is a standard approach in all areas of system identification, including patch clamp assessment of Cm (6).

Our dual-sine analysis fundamentally corrects for effects of Rs, since it works by finding the parameter solutions of the total admittance of the patch clamp-cell circuit (as modelled above), given a known voltage across the total admittance. Thus, Cm derivation by this method takes into account the voltage drop across Rs at any frequency, providing true measures of Cm across frequency. Fits to Cm-Vm (or Q-Vm, in the case of current integrations) are made using corrected Vm values based on measured Rs, namely, Vm= Vcom – Irs * Rs, where the cell has been held sufficiently long to reach steady state voltage levels (in our case, for hundreds of ms before Cm analysis). Below, we show with electrical and mathematical models that Rs effects do not interfere with our Cm measures.

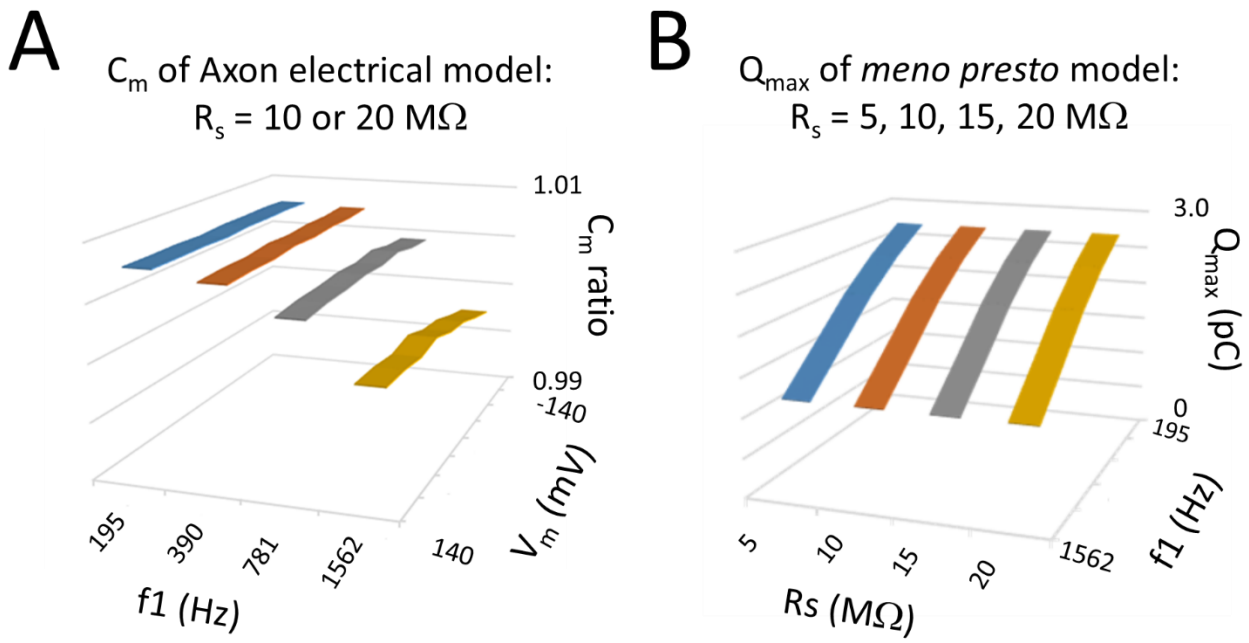

A) An electrical model cell was used to measure Cm, following stray capacitance cancellation as above. Model parameters were Rs=10 or 20MΩ, Rm = 500 MΩ, Cm= 33 pF. The plot shows that the ratios of Cm@20 MΩ/ Cm@10 MΩ measured at a range of holding potentials and frequencies (primary f1 frequency of dual-sine stimulus shown) are essentially identical (ratio ~ 1), regardless of Rs value. This indicates that Rs (with its influence on clamp time constant) does not affect our Cm frequency response measures in the absence of stray capacitance. Average Cm across voltages at 195 Hz was 33.0 pF for 10 MΩ Rs and 33.2 pF for 20 MΩ Rs. At 1562 Hz values were 33.1 pF for 10 MΩ Rs and 33.0 pF for 20 MΩ Rs. Differences arise form variability in stray capacitance cancellation, as is evident from model evaluations in B) in the absence of stray capacitance.

B) The *meno presto* model (7) was used to measure Cm-Vm functions that were fit to extract Qmax. Rs ranging from 5-20 MΩ has no effect on the magnitude *or* frequency response of NLC (Qmax), which is frequency-dependent due to model transition rates. Frequency is (plotted on a linear scale. Chloride set to 140 mM. Rm=200 MΩ, Clin=20 pF.

References

1. Santos-Sacchi, J. 2004. Determination of cell capacitance using the exact empirical solution of dY/dCm and its phase angle. Biophys J 87:714-727.
2. Santos-Sacchi, J., S. Kakehata, and S. Takahashi. 1998. Effects of membrane potential on the voltage dependence of motility-related charge in outer hair cells of the guinea-pig. J.Physiol 510 (Pt 1):225-235.
3. Ricci, A. J., J.-P. Bai, L. Song, C. Lv, D. Zenisek, and J. Santos-Sacchi. 2013. Patch-Clamp Recordings from Lateral Line Neuromast Hair Cells of the Living Zebrafish. Journal of Neuroscience 33:3131-3134.
4. Schnee, M. E., J. Santos-Sacchi, M. Castellano-Munoz, J. H. Kong, and A. J. Ricci. 2011. Calcium-dependent synaptic vesicle trafficking underlies indefatigable release at the hair cell afferent fiber synapse. Neuron 70:326-338.
5. Schnee, M. E., J. Santos-Sacchi, M. Castellano-Munoz, J. H. Kong, and A. J. Ricci. 2011. Tracking vesicle fusion from hair cell ribbon synapses using a high frequency, dual sine wave stimulus paradigm. Communicative & Integrative Biology 4:785-787.
6. Gillis, K. D. 1995. Techniques for Membrane Capacitance Measurements. In Single Channel Recording. B. Sakmann, and E. Neher, editors. Plenum Press, New York. 155-198.
7. Santos-Sacchi, J., and L. Song. 2014. Chloride and Salicylate Influence Prestin-dependent Specific Membrane Capacitance. Journal of Biological Chemistry 289:10823-10830.